JOURNAL OF Materials CHEMISTRY

Crystal structure and electronic properties of $Ca_4Mn_2TiO_{9.93}$, an $n=3$ Ruddlesden–Popper compound†‡

Peter D. Battle,[a] Stephen J. Blundell,[b] Amalia I. Coldea,[b] Edmund J. Cussen,[a]§ Matthew J. Rosseinsky,[a]§ John Singleton,[b] Lauren E. Spring[a] and Jaap F. Vente[a]¶

[a]*Inorganic Chemistry Laboratory, Oxford University, South Parks Road, Oxford, UK OX1 3QR*
[b]*Clarendon Laboratory, Oxford University, Parks Road, Oxford, UK OX1 3PU*

Received 22nd May 2000, Accepted 29th June 2000
First published as an Advance Article on the web 10th October 2000

Traditional solid state synthetic methods were used to prepare a polycrystalline sample of the $n=3$ Ruddlesden–Popper phase $Ca_4Mn_2TiO_{9.93}$. The crystal structure (space group *Pbca*, $a=5.31411(5)$, $b=5.31148(5)$, $c=26.9138(2)$ Å) was determined by the simultaneous analysis of neutron and X-ray diffraction data, with near-edge anomalous scattering being used to provide contrast between Mn and Ti cations. The latter show a small preference for the octahedral sites at the centre of the three-layer perovskite blocks within the structure. Neutron diffraction data collected at 5 K show no evidence for long-range magnetic ordering, although an enhanced magnetisation with a weak remanence is observed at low temperature; this is ascribed to the presence of antisymmetric exchange interactions. $Ca_4Mn_2TiO_{9.93}$ is a semiconductor with a temperature-dependent activation energy of $\sim$100 meV. Only weak ($\rho_B/\rho_0>0.9$ in 14 T at 75 K) magnetoresistance was observed.

Introduction

The magnetotransport properties of Mn-containing oxides have stimulated a great deal of research activity in recent years.[1,2] The majority of the compounds of interest show a spontaneous magnetisation at low temperatures and contain mixed-valence Mn^{3+}/Mn^{4+} cations in a perovskite-related crystal structure. It has been demonstrated that, in many cases, their resistivity at temperatures slightly above the Curie temperature (T_c) drops by several orders of magnitude on the application of a magnetic field. No adequate explanation of this negative colossal magnetoresistance (CMR; $(\rho_B-\rho_0)/\rho_0 \sim -0.99$ or $\rho_B/\rho_0 \sim 0.01$) behaviour is presently available, although it is generally agreed that double exchange[3] on the Mn sublattice is an important factor. However, models which rely on this mechanism cannot explain the observation[4] of CMR in the pyrochlore $Tl_2Mn_2O_7$, which, as an oxide of Mn^{4+}, does not have a non-integral number of electrons per Mn, as is required if the double exchange mechanism is to operate. The range of perovskite-related compounds which show the effect is not limited to those with a formula of the type ABO_3. It also includes[5,6] compounds having the formula $A_2A'B_2O_7$, that is the $n=2$ members of the Ruddlesden–Popper (RP) family[7] $(A,A')_{n+1}B_nO_{3n+1}$, where A and A′ are both large, electropositive cations. The perovskite ABO_3 is the $n=\infty$ end member of this family, all the members of which can be considered to consist of blocks of corner-sharing BO_6 octahedra which extend to infinity in the *xy* plane, and are *n* octahedra thick parallel to *z*; neighbouring blocks are separated by rock-salt layers, so that the formula can usefully be written as $((A,A')BO_3)_n(A,A')O$. We have previously reported[8] the crystal structure and magnetic properties[9] of an $n=3$ compound $Ca_4Mn_3O_{10}$. This material shows an orthorhombic distortion of the tetragonal structure usually associated with RP phases, and it orders as a weak ferromagnet at 115 K. However, despite the presence of a spontaneous magnetisation, magnetotransport measurements[10] revealed a level of magnetoresistance in this compound which, although significant ($\rho_B/\rho_0 \sim 0.6$ in 14 T at 61 K), was not as high as that seen in $n=2$ phases. We have subsequently[11] prepared the compounds $Ca_4Mn_2FeO_{10-\delta}$ and $Sr_4Mn_2FeO_{10-\delta}$ in order to ascertain whether the structural and electronic changes induced by the introduction of Fe can have a beneficial effect on the magnetotransport properties of the $n=3$ phases; the introduction of Fe^{4+} into an oxide of Mn^{4+} was intended to lead to the presence of both d^4 and d^3 cations, as is the case in the Mn^{3+}/Mn^{4+} oxides which show CMR. However, our aims were frustrated by the effects of both Mn/Fe and anion disorder, together with incomplete cation oxidation. We have now prepared and characterised a phase, $Ca_4Mn_2TiO_{10-\delta}$, in which 33% of the paramagnetic cations are replaced by diamagnetic Ti^{4+}. Our hope was that the Mn and Ti cations would order in such a way that the octahedral sites in the central layer of a perovskite block were occupied by Ti, with the sites in the two outer layers occupied by Mn. Conventional single-layer $n=1$ RP phases have previously[12] shown charge ordering and spin-glass behaviour rather than CMR, but we hoped that this new material containing single, magnetically-isolated layers of MnO_6 octahedra might act as a CMR material with appropriate doping. The synthesis and characterisation of this phase are described below. The structural part of this study is non-routine because neither conventional powder X-ray diffraction nor neutron diffraction can reliably distinguish between Ti and Mn; in both cases the scattering factors of the two elements are essentially the same. In order to introduce the necessary contrast into the diffraction experiment we have taken advantage of the tunability of synchrotron radiation to

†Basis of a presentation given at Materials Discussion No. 3, 26–29 September, 2000, University of Cambridge, UK.
‡Electronic supplementary information (ESI) available: anisotropic thermal parameters for $Ca_4Mn_2TiO_{9.93}$ at room temperature and 5 K. See http://www.rsc.org/suppdata/jm/b0/b003189p/
§Present address: Chemistry Department, Liverpool University, Liverpool, UK L69 7ZD.
¶Present address: Departamento de Fisica Aplicada, Cinvestav-IPN Unidad Mérida, Carretera Ant. a Progreso km 6, Apartado Postal #73 Cordemex, Mérida, Yucatan, 97310 México.

 DOI: 10.1039/b003189p

select an X-ray wavelength close to the absorption edge of Mn^{4+} (but not Ti^{4+}). The form factor of Mn^{4+} close to the edge can be written as $f=f_0+\Delta f'+if''$, where f_0 is the form factor away from the edge, and $\Delta f'$ and f'' are the real and imaginary anomalous contributions to the form factor close to the edge. The latter can be treated as a constant, whereas the former is a fast function of wavelength and can thus be used to introduce significant contrast between the scattering by two elements which have a similar number of electrons.[13] Our strategy was therefore to perform a structure refinement by simultaneously analysing neutron diffraction data and near-edge X-ray data, with the former providing vital information about the location of the light anions and the latter defining the distribution of the Ti and Mn cations; a set of X-ray data collected away from the edge was also included in the analysis.

Experimental

A polycrystalline sample ($\sim$5 g) of $Ca_4Mn_2TiO_{10-\delta}$ was prepared using standard ceramic techniques. Stoichiometric quantities of $CaCO_3$ (99.995%, Alfa), MnO_2 (99.999% Puratronic, Alfa) and TiO_2 (99.995% Puratronic, Alfa) were ground together thoroughly, pelletized, loaded into an alumina crucible and heated in air at temperatures of up to 1275 °C as described in Table 1. After the final firing the sample was cooled to 1200 °C at a rate of 5 °C min^{-1} and then air quenched to room temperature. The progress of the reaction was monitored using an in-house X-ray powder diffractometer. We were unable to determine the oxygen content of the sample reliably by chemical methods.

The final product was subjected to a more extensive X-ray examination using diffractometer 2.3 at the Daresbury Laboratory Synchrotron Radiation Source. Data were collected by stepping ($\Delta 2\theta=0.01°$) over the angular range $20\leqslant 2\theta/°\leqslant 120$ at nominal wavelengths of $\lambda=1.4000$ and 1.8930 Å, the latter value being chosen to lie close to the Mn K absorption edge. Data were also collected on $SrMnO_3$, a well-characterised[14] oxide known to contain six-coordinate Mn^{4+}. The data collected on this standard facilitated calibration of the anomalous contribution ($\Delta f'$) to the form factor of Mn^{4+} close to the absorption edge. The background fluorescence signal from the sample was compared with that from the standard in order to confirm that the absorption edges are essentially coincident in the two materials. Neutron powder diffraction data were collected on $Ca_4Mn_2TiO_{10-\delta}$ at 295 K and 5 K using the diffractometer D2b at the ILL, Grenoble. The sample was contained in a cylindrical vanadium can of diameter 8 mm and data were collected with $\lambda=1.5940$ Å, $8\leqslant 2\theta/°\leqslant 150$, $\Delta 2\theta=0.05°$.

Magnetisation data were collected on $Ca_4Mn_2TiO_{10-\delta}$ as a function of applied field and temperature using a Quantum Design MPMS SQUID magnetometer. $M(T)$ was measured in a field of 100 G whilst warming through the temperature range $5\leqslant T/K\leqslant 300$; data were collected after cooling in zero field (ZFC) and after cooling in the measuring field (FC). $M(H)$ was measured ($-20\leqslant H/kG\leqslant 20$) at temperatures of 300, 100, 30, 10 and 5 K (in that order) with field cooling between measurements; these temperatures were selected after examination of the $M(T)$ data. Magnetotransport data were collected on a sintered bar of dimensions $5\times 2\times 2$ mm using apparatus described elsewhere.[15] Standard four probe geometry was used, with the direct current ($\leqslant 50$ μA) perpendicular to the applied field. $\rho(T)$ was measured while cooling the material from room temperature to 4.2 K in zero field and ρ_B was then measured sequentially at temperatures of 75, 100, 150 and 200 ± 1 K over the field range $0\leqslant B/T\leqslant 14$; warming between temperatures was performed in zero field.

Table 1 Synthesis conditions for $Ca_4Mn_2TiO_{10-\delta}$

Temperature/°C	Firing time/h
800	36
1000	24
1200	60
1250	40
1275	84

Results

Structural chemistry

The analysis of the powder diffraction data was carried out using the GSAS program package.[16] In all cases the background level was modelled using a shifted Chebyshev polynomial, and the peak shapes were described by a pseudo-Voigt function. The neutron diffraction data collected at room temperature were used in a preliminary structure refinement. This gave no reliable information on the Mn/Ti distribution, but allowed us to deduce accurate unit cell parameters and structural parameters for the oxygen and calcium atoms. These parameters were then used in the analysis of the X-ray data collected at $\lambda=1.4000$ Å, the Mn/Ti distribution being assumed to be random. This strategy demonstrated that the nominal values of the neutron and X-ray wavelengths were self-consistent to four decimal places. Consideration of the peak positions in the X-ray data set collected on $Ca_4Mn_2TiO_{10-\delta}$ close to the absorption edge established the higher wavelength as 1.8930 Å, again in excellent agreement with the intended value. Having calibrated both of the X-ray wavelengths, the structure of $SrMnO_3$ was refined making simultaneous use of the two available data sets ($\lambda=1.4000$ and 1.8930 Å), the purpose being to determine a value for $\Delta f'$, the real part of the anomalous scattering close to the absorption edge. The imaginary contribution to the Mn^{4+} form factor at $\lambda=1.8930$ Å (f'') was calculated (using GSAS) to be 2.81 e^- per Mn^{4+} and was held constant at this value in the data analysis. Refinement of the usual profile parameters, atomic coordinates, isotropic temperature factors and (at the higher wavelength only) $\Delta f'$ resulted in the fitting parameters $R_{wpr}=6.00\%$ ($\lambda=1.4000$ Å), 7.03% ($\lambda=1.8930$ Å), 6.49% (combined) and $\chi^2=1.328$, with $\Delta f'$ taking a value of $-9.04(5)$ e^- per Mn^{4+}. The high-quality fits obtained for the two data sets demonstrate that the use of these values for $\Delta f'$ and f'' adequately accounts for the change in the form factor of Mn^{4+} when a wavelength close to the edge is selected; a similar value for $\Delta f'$ has been determined previously for Mn^{4+}.[17]

The room temperature structure of $Ca_4Mn_2TiO_{10-\delta}$ was then analysed in detail by means of a simultaneous refinement of three diffraction profiles, that is one neutron and two X-ray data sets. During these refinements, $\Delta f'$ was held constant at the value determined during the refinement of $SrMnO_3$. The preliminary analysis of the neutron dataset had shown that, like $Ca_4Mn_3O_{10}$, $Ca_4Mn_2TiO_{10-\delta}$ is modelled best using the orthorhombic space group *Pbca*. However, there were significant differences between the observed and calculated profiles when a single-phase model was used. Careful inspection of the data suggested the presence of a second phase related to the perovskite $CaMnO_{3-\delta}$.[18,19] Refinement of the concentration and unit cell parameters of an additional phase, formulated as $CaMn_{2/3}Ti_{1/3}O_{2.97}$ and with the atomic coordinates held constant at the values reported for $CaMnO_{2.97}$, resulted in a significant improvement in the fit; the concentration refined to a value of 1.13% by weight and the unit cell parameters to $a=5.316(1)$; $b=5.308(1)$; $c=7.528(1)$ Å in space group *Pbnm*. The overall stoichiometry of the reaction mixture dictates that if an $n=\infty$ RP phase is present, then there should be also a trace of RP material with $n<3$, but this was not detectable. The simultaneous use of three data sets in our final refinements made it possible to refine the fractional occupan-

Table 2 Structural parameters for $Ca_4Mn_2TiO_{9.93}$ at room temperature[a]

Atom	Site	Occupancy (%)	x	y	z	$U_{iso}/U_{eq}/Å^2$
Ca(1)	8c	100	0.5011(5)	0.4792(6)	0.07000(9)	0.0132
Ca(2)	8c	100	−0.0036(6)	0.0130(8)	0.20432(6)	0.0121
Mn(3)	4b	59.8(2.6)	0	1/2	0	0.0034(6)
Ti(4)	4b	40.2(2.6)	0	1/2	0	0.0034(6)
Mn(5)	8c	70.1(1.3)	0.4992(7)	0.0011(7)	0.14111(7)	0.0064(4)
Ti(6)	8c	29.9(1.3)	0.4992(7)	0.0011(7)	0.14111(7)	0.0064(4)
O(7)	8c	100	0.4425(3)	0.0017(5)	0.06987(9)	0.0036(4)
O(8)	8c	100	0.5432(5)	−0.0124(6)	0.21117(6)	0.0063(5)
O(9)	8c	96.3(8)	0.7809(7)	0.2210(6)	0.13265(9)	0.0143
O(10)	8c	100	0.2178(5)	0.7790(6)	0.14743(8)	0.0145
O(11)	8c	100	0.2874(6)	0.2909(6)	−0.00860(8)	0.0063(5)

[a] $a = 5.31411(5)$; $b = 5.31148(5)$; $c = 26.9138(2)$ Å; $V = 759.662(16)$ Å^3.

Table 3 Selected bond lengths (Å) and angles (°) for $Ca_4Mn_2TiO_{9.93}$ at 295 K[a]

Ca(1)–O(7)^{i}	2.555(5)	Ca(2)–O(8)^{i}	2.419(4)	Mn(3)[b]–O(7)	1.905(2) ×2
Ca(1)–O(7)^{ii}	2.793(5)	Ca(2)–O(8)^{ii}	2.915(4)	Mn(3)–O(11)	1.903(5) ×2
Ca(1)–O(7)^{iii}	2.361(3)	Ca(2)–O(8)^{iii}	2.805(6)	Mn(3)–O(11)	1.928(5) ×2
Ca(1)–O(7)^{iv}	2.959(3)	Ca(2)–O(8)^{iv}	2.536(6)	Mn(5)–O(7)	1.941(3)
Ca(1)–O(9)^{i}	2.633(4)	Ca(2)–O(8)^{v}	2.292(2)	Mn(5)–O(8)	1.901(3)
Ca(1)–O(9)^{ii}	2.415(4)	Ca(2)–O(9)^{i}	2.501(4)	Mn(5)–O(9)[c]	1.912(5)
Ca(1)–O(10)^{i}	3.024(4)	Ca(2)–O(9)^{ii}	2.880(4)	Mn(5)–O(9)	1.905(6)
Ca(1)–O(10)^{ii}	2.613(4)	Ca(2)–O(10)^{i}	2.297(4)	Mn(5)–O(10)[c]	1.912(6)
Ca(1)–O(11)^{i}	2.601(4)	Ca(2)–O(10)^{ii}	2.578(5)	Mn(5)–O(10)	1.881(5)
Ca(1)–O(11)^{ii}	3.093(4)				
Ca(1)–O(11)^{iii}	2.341(4)				
Ca(1)–O(11)^{iv}	2.666(4)				

O(7)–Mn(3)–O(7)	180	O(8)–Mn(5)–O(9)	92.6(2)
O(7)–Mn(3)–O(11)	89.7(1)	O(8)–Mn(5)–O(9)	90.8(2)
O(7)–Mn(3)–O(11)	88.8(1)	O(8)–Mn(5)–O(10)	89.1(2)
O(11)–Mn(3)–O(11)	89.02(4)	O(8)–Mn(5)–O(10)	90.9(2)
		O(9)–Mn(5)–O(9)	89.0(2)
O(7)–Mn(5)–O(8)	177.2(3)	O(9)–Mn(5)–O(10)	178.2(2)
O(7)–Mn(5)–O(9)	90.2(2)	O(9)–Mn(5)–O(10)	90.7(2)
O(7)–Mn(5)–O(9)	88.8(2)	O(9)–Mn(5)–O(10)	90.5(2)
O(7)–Mn(5)–O(10)	88.1(2)	O(9)–Mn(5)–O(10)	178.3(2)
O(7)–Mn(5)–O(10)	89.6(2)	O(10)–Mn(5)–O(10)	89.8(2)
Mn(3)–O(11)–Mn(3)	157.4(1)	Mn(5)–O(9)–Mn(5)	160.5(2)
Mn(3)–O(7)–Mn(5)	161.9(2)	Mn(5)–O(10)–Mn(5)	162.9(2)

[a] Superscripts relate to the oxygen atoms numbered as in Fig. 8(a) and (b). [b] Mn(3) is used as shorthand for Mn(3)/Ti(4) with fractional occupancies given in Table 2. [c] One of the two *trans* O(9), O(10) pairs.

cies of Mn^{4+} and Ti^{4+} over the six-coordinate 4b and 8c sites. There is a small excess of Ti on the 4b sites at the centres of the perovskite blocks, with a corresponding excess of Mn on the 8c sites which make up the outer layers of the blocks. Refinement of the oxygen site occupancies revealed incomplete occupation of the O(9) position; this is an equatorial anion site in the outer layer of the perovskite blocks. The composition of the majority phase deduced from these refinements is thus $Ca_4Mn_2TiO_{9.93}$. It follows that 0.14 moles of Mn^{3+} are present per mole of $Ca_4Mn_2TiO_{9.93}$ and this, together with the presence of the $CaMn_{2/3}Ti_{1/3}O_{2.98}$ impurity, introduces a small, unquantifiable error into the anomalous dispersion analysis. The majority of the atoms were modelled with isotropic thermal parameters, although an anisotropic model was used when trial refinements showed it to be necessary. The resultant (total) residual fit parameters in the three-histogram refinement were as follows: $R_{wp} = 6.62\%$, $R_p = 5.64\%$, DWd = 1.308 and $\chi^2_{red} = 1.25$. The refined values of the atomic coordinates are listed in Table 2 and the thermal parameters are available as ESI.‡ The corresponding bond lengths and bond angles are listed in Table 3. A polyhedral view of the structure is shown in Fig. 1 and the observed and calculated diffraction profiles are drawn in Fig. 2.

In the absence of low-temperature X-ray data, the Mn/Ti distribution established at room temperature was carried

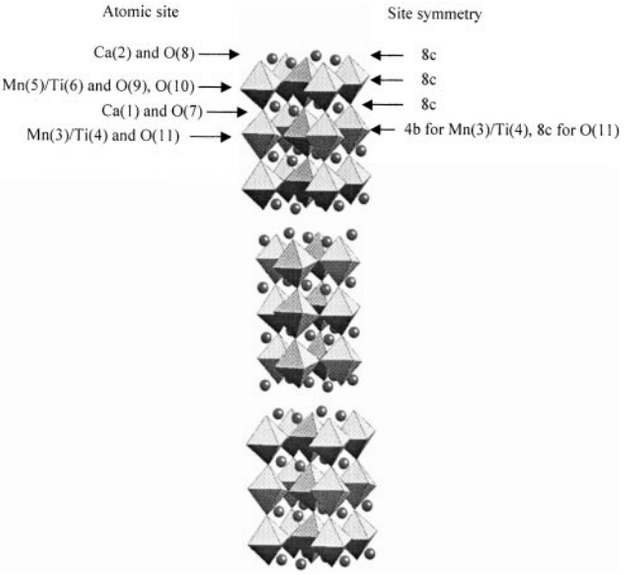

Fig. 1 Polyhedral representation of the crystal structure of the orthorhombic $n = 3$ Ruddlesden–Popper phase $Ca_4Mn_3O_{10}$.

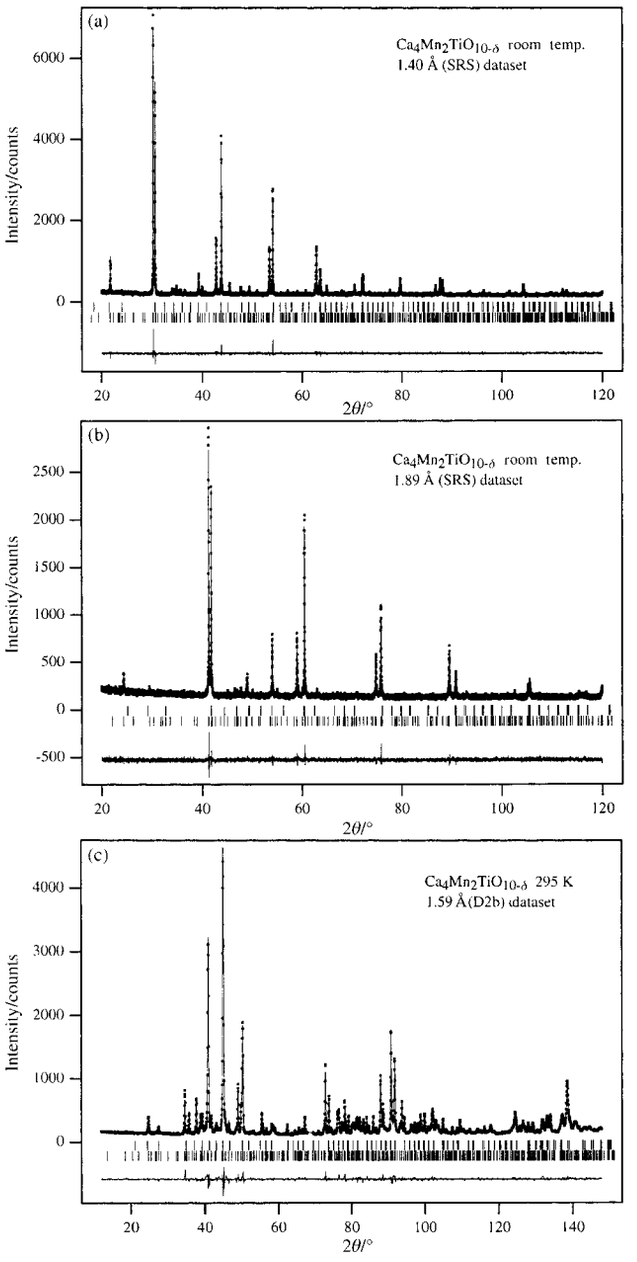

Fig. 2 Observed, calculated and difference diffraction profiles for $Ca_4Mn_2TiO_{9.93}$ at 295 K: (a) X-rays, $\lambda = 1.4000$ Å, (b) X-rays, $\lambda = 1.8930$ Å, (c) neutrons. Reflection positions for the minority (upper) and majority (lower) phases are marked.

through to the analysis of the neutron diffraction data collected at 5 K. The fitting parameters resulting from the single-histogram Rietveld refinement of the crystal structure of $Ca_4Mn_2TiO_{9.93}$ at 5 K were as follows: $R_{wp} = 5.63\%$, $R_p = 4.32\%$, DWd = 0.482 and $\chi^2_{red} = 6.232$. No magnetic Bragg peaks were apparent in the data collected at low temperature. The refined atomic coordinates are listed in Table 4, the thermal parameters are available as ESI,‡ and the most important bond lengths are given in Table 5. The observed and calculated diffraction profiles are drawn in Fig. 3.

Magnetism and magnetotransport

The temperature dependence of the molar magnetic susceptibility, defined as M/H, of $Ca_4Mn_2TiO_{9.93}$ is shown in Fig. 4. Above 245 K the data can be fitted to a Curie–Weiss Law with $C_m = 4.70(6)$ cm^3 K mol^{-1}, $\theta = -365(9)$ K; this value of the Curie constant is greater than the spin-only value (3.91 cm^3 K mol^{-1}). The molar magnetisation is clearly enhanced in the temperature range $5 < T/K < 70$. Comparison of the ZFC and FC signals shows the presence of hysteresis below 13 K, and both show a local maximum at ~8 K. The field dependence of the magnetisation at five selected temperatures is shown in Fig. 5. At 300, 100 and 30 K, $M(H)$ is linear, with no hysteresis evident. However, at 10 K and 5 K the linearity is lost, and hysteresis is observed at low fields; $M(H)$ remains symmetrical about the origin.

The magnetotransport behaviour of $Ca_4Mn_2TiO_{9.93}$, as a function of field at four different temperatures, is shown in Fig. 6. The sample resistance was immeasurably high (~300 MΩ) below 70 K. It proved possible to model the temperature dependence of the resistivity of $Ca_4Mn_2TiO_{9.93}$ in the temperature regions $125 < T/K < 295$ and $77 < T/K < 123$ using a simple activated conduction law $\rho \propto \exp(E_A/kT)$ with $E_A = 126.75(5)$ and 96.5(1) meV respectively.

Discussion

Partial (33%) substitution of Ti for Mn in $Ca_4Mn_3O_{10}$ results in the retention of orthorhombic symmetry, in contrast to Fe substitution which restores the ideal tetragonal symmetry of the $n = 3$ RP phase, albeit with the introduction of positional disorder on the anion sublattice; this disorder is not seen in $Ca_4Mn_2TiO_{9.93}$. Whereas the Fe cations showed a significant preference for the sites at the centre of the perovskite blocks in $Ca_4Mn_2FeO_{9.75}$, the degree of cation ordering in the Ti-doped material is only significant at the 2σ level, with the dopant again preferring the central layer. The octahedra in the central layer of the perovskite blocks of $Ca_4Mn_2TiO_{9.93}$ are larger and less regular than those in the undoped sample. The increase in the mean bond length from 1.899 Å to 1.912 Å can simply be attributed to the relatively large ionic radius of Ti^{4+}, but the anisotropic nature of the increase is interesting. In $Ca_4Ti_3O_{10}$[20] and $Ca_4Mn_3O_{10-\delta}$ the Mn–O distances in these centrosymmetric, central octahedra are all equal (within σ), whereas in $Ca_4Mn_2TiO_{9.93}$ although the lengths of the two apical Mn/Ti–O(7) bonds and two of the equatorial Mn/Ti–O(11) bonds are essentially the same (~1.90 Å), the other pair of Mn/Ti–O(11)

Table 4 Structural parameters for $Ca_4Mn_2TiO_{9.93}$ at 5 K

Atom	Site	Fraction (%)	x	y	z	U_{iso}/U_{eq}/Å^2
Ca(1)	8c	100	0.5015(9)	0.476(1)	0.0699(3)	0.0084
Ca(2)	8c	100	−0.004(1)	0.015(2)	0.2041 (2)	0.0082
Mn(3)	4b	59.8(2.6)	0	1/2	0	0.000(2)
Ti(4)	4b	40.2(2.6)	0	1/2	0	0.000(2)
Mn(5)	8c	70.1(1.3)	0.503(2)	0.009(2)	0.1410(3)	0.003(1)
Ti(6)	8c	29.9(1.3)	0.503(2)	0.009(2)	0.1410(3)	0.003(1)
O(7)	8c	100	0.4403(6)	0.0019(8)	0.0701(2)	−0.0005(8)
O(8)	8c	100	0.5455(9)	−0.013(1)	0.2113(1)	0.001(1)
O(9)	8c	96.3(8)	0.783(1)	0.222(1)	0.1322(2)	0.0085
O(10)	8c	100	0.2158(9)	0.778(1)	0.1476(2)	0.0101
O(11)	8c	100	0.285(1)	0.294(1)	−0.0092(2)	0.003(1)

[a] $a = 5.3050(1)$; $b = 5.3047(1)$; $c = 26.8619(6)$ Å; $V = 755.93(5)$ Å^3.

Table 5 Selected bond lengths (Å) for $Ca_4Mn_2TiO_{9.93}$ at 5 K[a]

Ca(1)–O(7)^{i}	2.54(1)	Ca(2)–O(8)^{i}	2.401(7)	Mn(3)^{b}–O(7)	1.910(5) ×2
Ca(1)–O(7)^{ii}	2.81(1)	Ca(2)–O(8)^{ii}	2.926(7)	Mn(3)–O(11)	1.881(8) ×2
Ca(1)–O(7)^{iii}	2.348(5)	Ca(2)–O(8)^{iii}	2.82(1)	Mn(3)–O(11)	1.948(7) ×2
Ca(1)–O(7)^{iv}	2.964(5)	Ca(2)–O(8)^{iv}	2.52(1)	Mn(5)–O(7)	1.932(8)
Ca(1)–O(9)^{i}	2.619(8)	Ca(2)–O(8)^{v}	2.292(5)	Mn(5)–O(8)	1.906(8)
Ca(1)–O(9)^{ii}	2.408(8)	Ca(2)–O(9)^{i}	2.492(8)	Mn(5)–O(9)^{c}	1.88(1)
Ca(1)–O(10)^{i}	3.036(8)	Ca(2)–O(9)^{ii}	2.889(8)	Mn(5)–O(9)	1.91(1)
Ca(1)–O(10)^{ii}	2.607(8)	Ca(2)–O(10)^{i}	2.290(8)	Mn(5)–O(10)^{c}	1.96(1)
Ca(1)–O(11)^{i}	2.605(8)	Ca(2)–O(10)^{ii}	2.567(8)	Mn(5)–O(10)	1.85(1)
Ca(1)–O(11)^{ii}	3.108(7)				
Ca(1)–O(11)^{iii}	2.330(8)				
Ca(1)–O(11)^{iv}	2.639(8)				

[a]Superscripts relate to the oxygen atoms numbered as in Fig. 8(a) and (b). [b]Mn(3) is used as shorthand for Mn(3)/Ti(4) with fractional occupancies given in Table 2. [c]One of the two *trans* O(9), O(10) pairs.

distances are significantly longer (~1.93 Å). The origin of this distortion is unclear. The mean Mn/Ti–O bond length in the outer octahedra is 1.909 Å, lower than that in the central octahedra, and thus consistent with the outer site holding a lower concentration of the larger Ti^{4+} cations. The outer octahedra in $Ca_4Mn_2TiO_{9.93}$ are less regular than the central octahedra, a pattern which was also observed in the cases of $Ca_4Ti_3O_{10}$ and $Ca_4Mn_3O_{10-\delta}$. However, the nature of the irregularity is different. Whereas in $Ca_4Ti_3O_{10}$ and $Ca_4Mn_3O_{10-\delta}$ the *trans* equatorial bonds in the outer layer

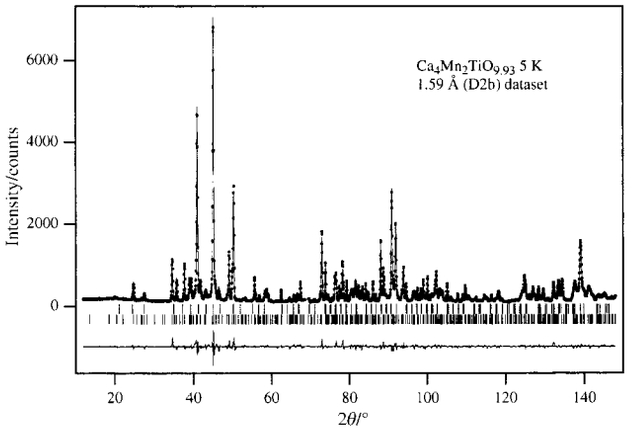

Fig. 3 Observed, calculated and difference neutron diffraction profiles for $Ca_4Mn_2TiO_{9.93}$ at 5 K. Reflection positions for the minority (upper) and majority (lower) phases are marked.

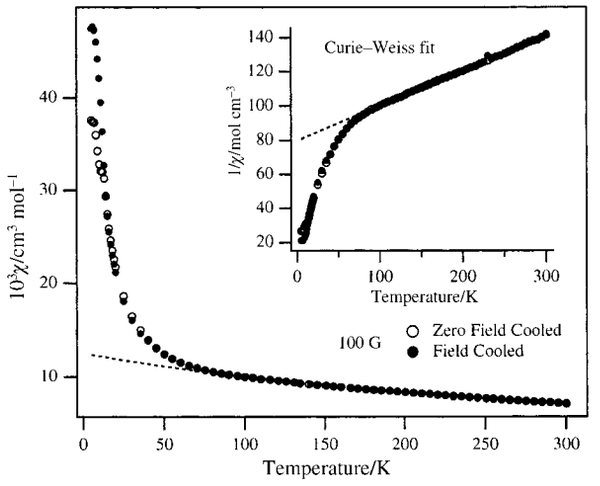

Fig. 4 Molar magnetic susceptibility of $Ca_4Mn_2TiO_{9.93}$ as a function of temperature, measured in a field of 100 G; the inset shows a fit of the inverse susceptibility to the Curie–Weiss law. Fit parameters are given in the text.

differ significantly from each other in length, such that the cation can be considered to be displaced from the centre of the octahedron, in $Ca_4Mn_2TiO_{9.93}$ three of the four equatorial bonds are essentially equal (~1.91 Å), with one Mn/Ti–O(10) distance (1.881 Å) being significantly shorter. As in $Ca_4Ti_3O_{10}$ and $Ca_4Mn_3O_{10-\delta}$, the length of the apical Mn/Ti–O(8) bond extending from the outer octahedron into the rocksalt layer is shorter than the *trans* Mn/Ti–O(7) bond directed into the perovskite block. The magnitude of this asymmetry, the origin of which has been discussed previously,[8] increases with increasing Ti content in the three compounds under discussion; this is consistent with the known bonding properties of the Ti^{4+}: $3d^0$ cation, which favours asymmetric coordination with multiple bonding to oxygen. Although there is a considerable spread among the Mn/Ti–O distances, the *cis* Mn–O–Mn bond angles are all close to 90°. However, the *trans* Mn–O–Mn angles are typically ~160°, and the relative rotation of neighbouring octahedra illustrated in Fig. 7 is a significant aspect of the orthorhombic distortion, being comparable in magnitude to that seen in $Ca_4Mn_3O_{10}$. The refined oxygen vacancy concentration allows the presence of 0.14 moles of the Mn^{3+}: $3d^4$ cation per mole of $Ca_4Mn_2TiO_{9.93}$. This Jahn–Teller ion might be expected to occupy preferentially the outer octahedra of the triple layer, where the inherent lack of symmetry facilitates a distorted geometry. This would be consistent with the concentration of the oxide anion vacancies on the O(9) site in this layer and the fact that the thermal parameters (Table 2) of the atoms in and around the outer layer of the perovskite blocks (Ca(1), Ca(2), Mn(5), O(9), O(10)) are larger than those of the atoms located within the central layer (O(11), Mn(3)). The tilting of the Mn/Ti polyhedra is largely responsible for the irregularity of the coordination geometry around the calcium sites illustrated in Fig. 8. In an ideal $n=3$ RP structure, the Ca(1) cation in the perovskite block of $Ca_4Mn_2TiO_{9.93}$ would be 12-coordinate, but in $Ca_4Mn_2TiO_{9.93}$ only ten anions lie within 3 Å of the Ca(1) site. However, the Ca(2) site within the rock-salt layer achieves the ideal coordination number of nine within a radius of 2.915(4) Å. We have previously argued[8,11] that the orthorhombic distortion of the ideal $n=3$ structure in the case of $Ca_4Mn_3O_{10}$ is driven by the need to satisfy the coordination requirements of Ca^{2+}, and that the absence of such a distortion in $Ca_4FeMn_2O_{10}$ can be attributed to the high concentration of Jahn–Teller active Fe^{4+}: $3d^4$ cations which produce the necessary distortions locally, without a cooperative phase change. This is consistent with the observation of orthorhombic symmetry in $Ca_4Mn_2TiO_{9.93}$, which has only a low concentration of Jahn–Teller cations.

The crystal structure of $Ca_4Mn_2TiO_{9.93}$ undergoes a number of modifications on cooling to 5 K. The mean Mn/Ti–O bond distance in the central octahedron does not change significantly, but the mismatch between the *cis* bonds to O(11) within the equatorial plane becomes more pronounced. Neither does

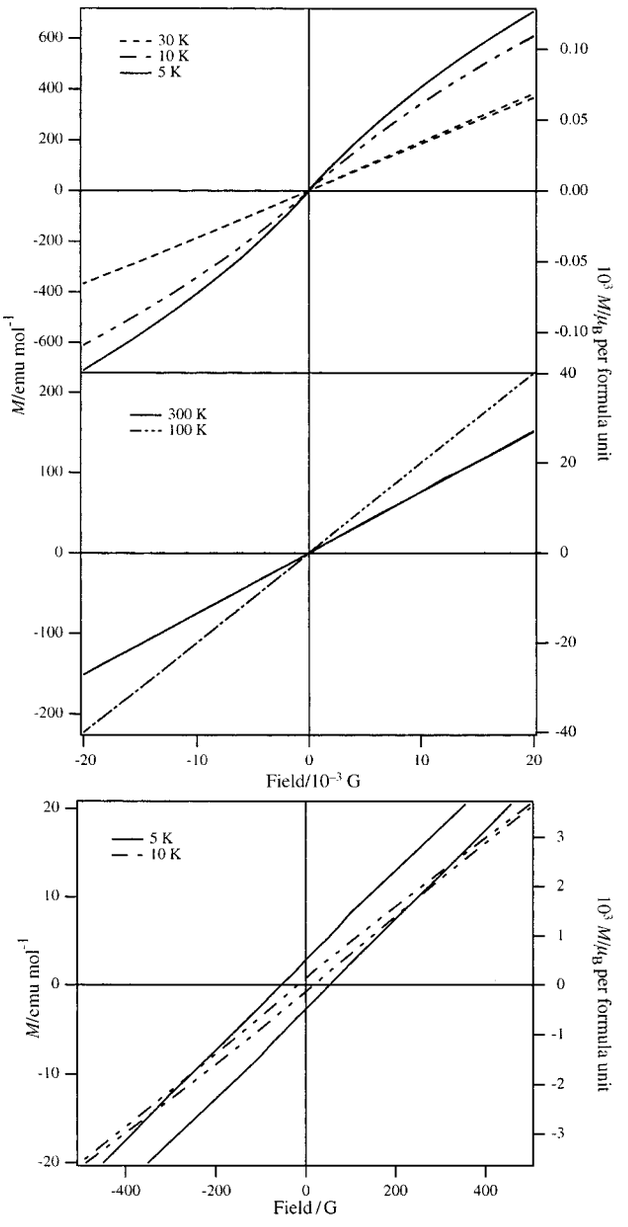

Fig. 5 (a) Field dependence of magnetisation of $Ca_4Mn_2TiO_{9.93}$ for $-20 \leqslant H/\mathrm{kG} \leqslant 20$, at temperatures of 300, 100, 30, 10 and 5 K. (b) Field dependence of magnetisation of $Ca_4Mn_2TiO_{9.93}$ for $-0.5 \leqslant H/\mathrm{kG} \leqslant 0.5$, at temperatures of 10 and 5 K.

the mean Mn/Ti–O bond length (1.91 Å) in the outer octahedron change, but the cation is now clearly displaced from the centre of the octahedron along each of the three axes, thus increasing the structural similarity with $Ca_4Ti_3O_{10}$ and $Ca_4Mn_3O_{10-\delta}$. One of the Mn/Ti–O(10) bond lengths is consequently reduced to 1.85(1) Å, a short distance which is consistent with the presence of a relatively high Mn concentration on this site. All of the thermal parameters are reduced on cooling, but those of Ca(1), Ca(2), O(9) and O(10) remain large enough to suggest that local static disorder is present at these sites.

The magnetic properties of $Ca_4Mn_2TiO_{9.93}$ differ markedly from those of $Ca_4Mn_2FeO_{9.75}$ and $Ca_4Mn_3O_{10-\delta}$, both of which show G-type antiferromagnetic order within the perovskite block (although for the Fe compound the central layer of manganese-poor octahedra remained magnetically disordered). In contrast, the absence of magnetic Bragg scattering in the neutron diffraction pattern collected at 5 K shows that long range magnetic order is not present in $Ca_4Mn_2TiO_{9.93}$. However, the temperature and field dependences of the magnetisation demonstrate that the sample is not a simple paramagnet. It is instructive to review the magnetic

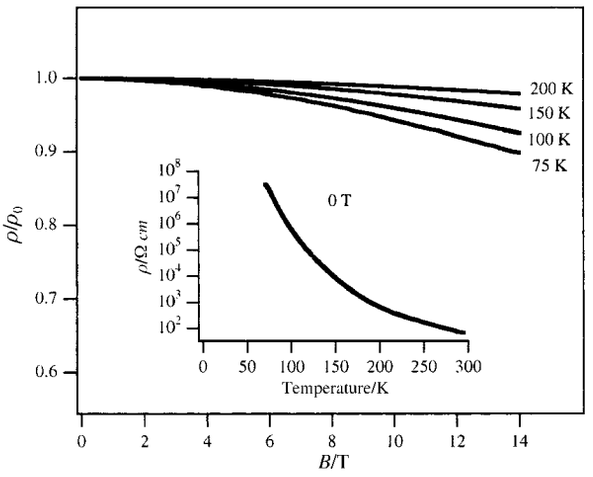

Fig. 6 Field dependence of normalised resistivity $\rho(B)/\rho(0)$ of $Ca_4Mn_2TiO_{9.93}$ at temperatures of 200, 150, 100 and 75 K. The inset shows the temperature dependence of resistivity at zero field.

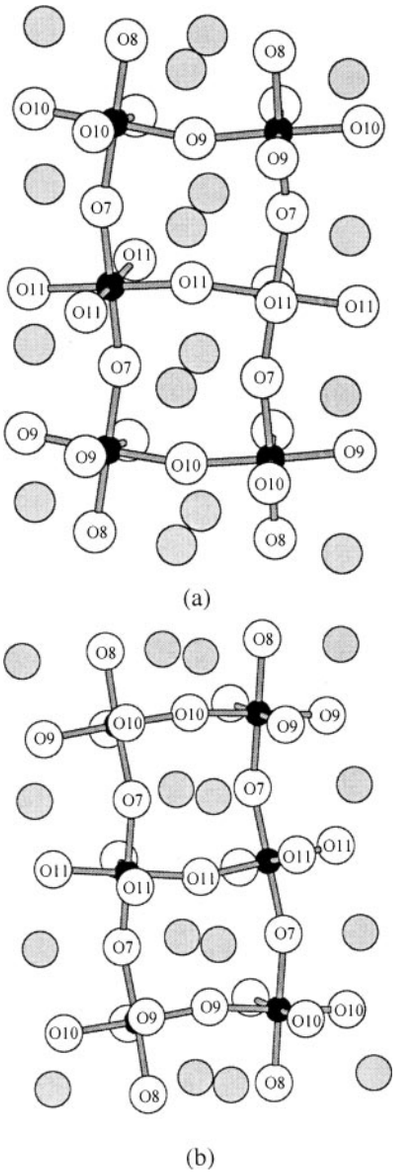

Fig. 7 Tilting of Mn/TiO_6 octahedra viewed along directions close to (a) [110] and (b) [1$\bar{1}$0]

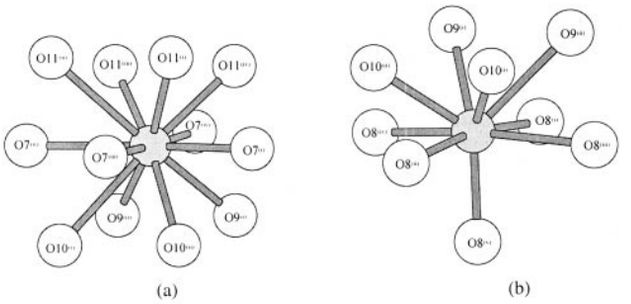

Fig. 8 Coordination geometry around the cations (a) Ca(1) and (b) Ca(2) in $Ca_4Mn_2TiO_{9.93}$ at room temperature.

exchange interactions present in each of the three compounds in order to rationalise the differences in magnetic behaviour. The observation of insulating, rather than metallic, behaviour in each case precludes any significant contribution from double exchange. Orthorhombic $Ca_4Mn_3O_{10-\delta}$ has been[9] shown to undergo a transition to a weakly ferromagnetic state at $\sim$115 K, the spontaneous magnetisation (2×10^{-3} μ_B per Mn at 5 K in 500 G) developing as a result of antisymmetric exchange (the Dzyaloshinski–Moriya (DM) mechanism[21,22]). However, in this compound the antiferromagnetic t_{2g}–t_{2g} π interactions between Mn^{4+}: $3d^3$ cations are dominant. In $Ca_4Mn_2FeO_{9.75}$, in addition to the antiferromagnetic t_{2g}–t_{2g} π interactions between Mn^{4+} cations, there will be competing, ferromagnetic superexchange interactions between a half-occupied e_g orbital on Fe^{4+} (or the small amount of Fe^{3+} present) and an empty e_g orbital on Mn^{4+}. However, the tetragonal symmetry of this compound prohibits a ferromagnetic DM interaction. The Fe^{4+}/Fe^{3+} distributions in this compound were shown[11] to be influential in determining which of the competing magnetic interactions predominated. No ordered moment was observed on the Fe-rich octahedral sites in the central layer of the perovskite block, suggesting overall frustration of the interactions between the Mn^{4+}: d^3 and Fe^{4+}: d^4 cations. However, with Fe^{n+} occupying only $\sim$21% of the octahedra in the outer layer of the perovskite block, antiferromagnetic t_{2g}–t_{2g} π interactions between Mn^{4+} cations predominate and G-type ordering is established in these layers. With these observations in mind, the competing interactions within a Mn^{4+} cation array which has been diluted with diamagnetic Ti^{4+}: d^0 cations, can be evaluated. We expect the antiferromagnetic π interactions between the numerous Mn^{4+} cations to dominate, although some ferromagnetic Mn^{3+} t_{2g}^3 e_g^1–O^{2-}–Mn^{4+} t_{2g}^3 σ superexchange interactions will also be present as a result of oxygen non-stoichiometry. The dilution of the dominant antiferromagnetic interactions may be considered to be exacerbated by the low degree of Mn/Ti ordering over the two transition metal sites, in that whereas the preference of the Fe cations for the central layer of octahedra in $Ca_4FeMn_2O_{10}$, and the correspondingly low Fe concentration in the outer octahedra, permitted a solid solution with $\sim$78% Mn occupation to preserve a magnetically ordered backbone on the latter sites, the reduction of the Mn concentration to $\sim$60% and $\sim$70% respectively in the inner and outer layers of $Ca_4Mn_2TiO_{9.93}$ prevents the onset of long-range magnetic order. However, these concentrations are both well in excess of the percolation limit, and it is likely that other factors are also at work. These could include the modifications to the superexchange interactions which will be caused by the structural distortions present in the Mn/TiO_6 network. However, next-nearest-neighbour (NNN) interactions are likely to be a more significant factor. It has been shown[23,24] that 50% dilution of the magnetic sublattice of a perovskite ($n=\infty$ RP) by d^0 cations results in the formation of a spin glass with $T_g\sim20$ K. Given the non-frustrated topology of the perovskite structure, this behaviour is usually ascribed to competition between nearest neighbour (NN) interactions and the weaker but more numerous NNN interactions. Furthermore, it has been shown that the NNN interactions are relatively strong when the magnetic cation has a d^3 electron configuration[25] and it is therefore reasonable to postulate that competition between NN and NNN superexchange interactions over a 33% diluted Mn^{4+}: $3d^3$ magnetic sublattice in a structure which is intermediate between 2- and 3-dimensional prevents the onset of long-range magnetic order.

Although magnetic ordering is not observed by powder neutron diffraction above 5 K, the Curie–Weiss parameters deduced from the high temperature region of the susceptibility data demonstrate that strong intercation magnetic interactions are present in orthorhombic $Ca_4Mn_2TiO_{9.93}$ throughout the measured temperature range. The large, negative Weiss constant indicates that these short-range interactions are predominantly antiferromagnetic above 100 K, but the enhancement of the susceptibility observed below this temperature indicates that, in some way or other, local regions within the sample develop an enhanced magnetisation. The data show a transition at 13 K, and the presence of a remanent magnetisation below this temperature. The symmetrical disposition of the hysteresis loop about the origin suggests the presence of a weak ferromagnetism rather than a spin glass phase; this contrasts with the case of tetragonal $Ca_4FeMn_2O_{10}$, where displaced hysteresis loops were observed. The magnitude of the magnetisation per Mn cation at 5 K and 500 G is comparable to that produced by antisymmetric exchange in orthorhombic $Ca_4Mn_3O_{10-\delta}$. It has been shown[9] that this weak DM magnetisation persists within the perovskite blocks of $Ca_4Mn_3O_{10-\delta}$ above the temperature of the transition to a phase showing long-range, 3D magnetic ordering. We therefore propose that at high temperatures, antiferromagnetic Mn–O–Mn interactions within the perovskite blocks dominate the short-range magnetism of $Ca_4Mn_2TiO_{9.93}$, but that below $\sim$100 K the consequences of the antisymmetric DM exchange become observable, with the magnetisation vector produced by the non-linear Mn–O–Mn interactions within each block being aligned with those of neighbouring blocks by the applied field. We envisage the antiferromagnetically coupled spin components to lie within the perovskite layers, as they do in both $Ca_4Mn_3O_{10-\delta}$ and $Ca_4FeMn_2O_{10}$, and the net magnetisation to lie perpendicular to the layers, as was assumed (though not proved) in the case of $Ca_4Mn_3O_{10-\delta}$. In order for this model to be valid, any antiferromagnetic interblock coupling between the z components of the moment must be weaker than is the case in $Ca_4Mn_3O_{10-\delta}$ in order to allow the alignment of the DM moment by relatively weak fields. This is consistent with the absence of a long-range antiferromagnetic backbone at low temperatures. The nature of the transition at 13 K is still unexplained. It is possible that it corresponds to spontaneous alignment of the weak ferromagnetic moments, which are certainly too weak to be detected by neutron diffraction. Alternatively, the irreversibility of magnetic behaviour may be evidence for the blocking of clusters of spins below a temperature of $\sim$13 K. $Ca_4Mn_2TiO_{9.93}$ would benefit from more extensive characterisation by magnetometry and μSR spectroscopy in order to establish the true nature of the magnetic ground state. It is striking that the introduction of Ti^{4+}, merely a non-magnetic diluant, has a more dramatic effect on the magnetic properties of $Ca_4Mn_3O_{10-\delta}$ than does Fe^{4+}, a magnetic cation which introduces competing superexchange interactions. This may stem from the introduction of Ti=O bonds, and the consequent change in the electron density distribution within the crystal. Note that it has been assumed throughout this discussion of the magnetic behaviour of the sample that there is no contribution from the low-level $CaMn_{2/3}Ti_{1/3}O_{2.98}$ impurity.

The magnetotransport behaviour of the Ti-doped phase shows the insulating behaviour characteristic of a localised-

electron system. The value $E_A = 126.75$ meV measured in the temperature range $125 \leqslant T/K \leqslant 295$ is more typical of an $n = 2$, rather than an $n = 3$, layered manganite.[26] This gives some idea of the narrowing of the bandwidth which occurs on introducing the Ti dopant into the Mn–O network. Energy fluctuations caused by the randomness of the chemical substitution and the concomitant crystallographic distortions will both play a rôle in carrier localisation, but it is noteworthy that the activation energy is reduced in the temperature region where the magnetisation is enhanced. Given that negative magnetoresistance is often associated with the presence of ferromagnetic coupling, it may be significant that the magnitude of the effect in $Ca_4Mn_2TiO_{9.93}$ is comparable to that observed in $Ca_4Mn_3O_{10-\delta}$ above the magnetic ordering temperature (115 K) when each perovskite block carries a weak DM magnetisation, but the interblock coupling of the atomic moments is negligible, that is when the situation is directly comparable to that found in $Ca_4Mn_2TiO_{9.93}$ over a wide temperature range. We take this as evidence in support of the model of the magnetic behaviour proposed above.

Acknowledgements

We are grateful to EPSRC, Oxford University and (AIC) the ORS Award Scheme for financial support.

References

1 R. M. Kusters, J. Singleton, D. A. Keen, R. McGreevy and W. Hayes, *Physica B*, 1989, **155**, 363.
2 A. P. Ramirez, *J. Phys.: Condens. Matter*, 1997, **9**, 8171.
3 C. Zener, *Phys. Rev.*, 1951, **82**, 403.
4 Y. Shimakawa, Y. Kubo and T. Manako, *Nature*, 1996, **379**, 53.
5 P. D. Battle, S. J. Blundell, M. A. Green, W. Hayes, M. Honold, A. K. Klehe, N. S. Laskey, J. E. Millburn, L. Murphy, M. J. Rosseinsky, N. A. Samarin, J. Singleton, N. A. Sluchanko, S. P. Sullivan and J. F. Vente, *J. Phys.: Condens. Matter*, 1996, **8**, L427.
6 Y. Moritomo, A. Asamitsu, H. Kuwahara and Y. Tokura, *Nature*, 1996, **380**, 141.
7 S. N. Ruddlesden and P. Popper, *Acta Crystallogr.*, 1958, **11**, 541.
8 P. D. Battle, M. A. Green, J. Lago, J. E. Millburn, M. J. Rosseinsky and J. F. Vente, *Chem. Mater.*, 1998, **10**, 658.
9 J. Lago, P. D. Battle and M. J. Rosseinsky, *J. Phys.: Condens. Matter*, 2000, **12**, 2505.
10 A. I. Mihut, L. E. Spring, R. I. Bewley, S. J. Blundell, W. Hayes, T. Jestädt, B. W. Lovett, R. McDonald, F. L. Pratt, J. Singleton, P. D. Battle, J. Lago, M. J. Rosseinsky and J. F. Vente, *J. Phys.: Condens. Matter*, 1998, **10**, L727.
11 P. D. Battle, W. R. Branford, A. Mihut, M. J. Rosseinsky, J. Singleton, J. Sloan, L. E. Spring and J. F. Vente, *Chem. Mater.*, 1999, **11**, 674.
12 J. C. Bouloux, J. L. Soubeyroux, A. Daoudi and G. L. Flem, *Mater. Res. Bull.*, 1981, **16**, 855.
13 M. A. G. Aranda, D. C. Sinclair, J. P. Attfield and A. P. Mackenzie, *Phys. Rev. B*, 1995, **51**, 12747.
14 P. D. Battle, T. C. Gibb and C. W. Jones, *J. Solid State Chem.*, 1988, **74**, 60.
15 L. E. Spring, D. Phil. Thesis, 1999, Oxford University, Oxford, UK.
16 A. C. Larson and R. B. von Dreele, General Structure Analysis System (GSAS), Los Alamos National Laboratories, Report LAUR 86-748, 1990.
17 Y. Murakami, H. Kawada, H. Kawata, M. Tanaka, T. Arima, Y. Moritomo and Y. Tokura, *Phys. Rev. Lett.*, 1998, **80**, 1932.
18 K. R. Poeppelmeier, M. E. Leonowicz, J. C. Scanlon, W. B. Yelon and J. M. Longo, *J. Solid State Chem.*, 1982, **45**, 71.
19 H. Taguchi, *J. Solid State Chem.*, 1996, **124**, 360.
20 M. M. Elcombe, E. H. Kisi, K. D. Hawkins, T. J. White, P. Goodman and S. Matheson, *Acta Crystallogr., Sect. B*, 1991, **47**, 305.
21 I. Dzyaloshinski, *J. Phys. Chem. Solids*, 1958, **4**, 241.
22 T. Moriya, *Phys. Rev.*, 1960, **120**, 91.
23 P. D. Battle, T. C. Gibb, A. J. Herod, S.-H. Kim and P. H. Munns, *J. Mater. Chem.*, 1995, **5**, 865.
24 E. J. Cussen, J. F. Vente, P. D. Battle and T. C. Gibb, *J. Mater. Chem.*, 1997, **7**, 459.
25 P. D. Battle, J. B. Goodenough and R. Price, *J. Solid State Chem.*, 1983, **46**, 234.
26 A. I. Coldea, L. E. Spring, S. J. Blundell, J. Singleton and W. Hayes, *J. Phys.: Condens. Matter*, 1999, **11**, 674.